

Variable emissivity through multilayer patterned surfaces for passive thermal control: preliminary thermal design of a nano-satellite

Athanasopoulos N.¹ and Siakavellas J. N.²

Department of Mechanical Engineering & Aeronautics, University of Patras, Patras, 26500

We have developed patterned surfaces that control the thermal radiation without the use of controllers and power supplies. Ultralight patterned surfaces were designed to passively transform their geometry and change their effective emissivity as a function of temperature with the purpose of controlling the temperature of a satellite. These transformable patterned surfaces may consist of flat smaller arrays, passively reacting under temperature stimuli by reversibly transforming their geometry from 2D to 3D complex shapes. The transformation of the arrays conceals or reveals materials of different thermo-optical properties, while the view factor of the surface changes as well. Consequently, the entire emissivity function of a surface can be designed. The shape transformation is attributed to the anisotropic properties of a tri-layer material and to the coefficient of thermal expansion mismatch, which cause the patterns to transform at any temperature level. We developed a low-cost tri-layer material that has been optimized to achieve very large deformations within small temperature deviations. The emissivity of the patterned surface presents significant variation, namely $\Delta\varepsilon \approx 0.7$ within $\Delta T \leq 40$ °C. The weight of the smart surfaces is less than 330 gr/m². The results are very promising because the degradation of the multilayer material of a unitary cell is negligible up to 78,000 thermal cycles. However, local degradation of the multilayer materials was observed near $N \approx 132,000$ thermal cycles due to local imperfections. The predicted and measured emissivity functions that we obtained were used for the preliminary thermal design of a nano-satellite in order to re-calculate its temperature (worst hot- and cold-cases) while taking into consideration different scenarios. The temperature deviation of the nano-satellite, as well as the minimum temperature, had significantly improved. The proposed re-design will have an advantageous impact on the selection of the heaters and the energy demands of a nano-satellite.

Nomenclature

A	=	Area
J	=	Radiosity
F	=	View factor
G_m	=	Mutual irradiation
T	=	Temperature
σ	=	Stefan Boltzmann constant
t	=	Time
ε_{eff}	=	Effective emissivity
a_{eff}	=	Effective absorptivity
Q	=	Heat flux
V	=	Voltage
I	=	Electrical current
$\Delta\lambda$	=	Distance from the laser device
I_S	=	Solar flux
I_E	=	Earth IR flux
\dot{Q}	=	Internal heat dissipation

¹ Postdoctoral Fellow, Department of Mechanical Engineering & Aeronautics, University of Patras, 26500 Patras, Greece, nathan@mech.upatras.gr, nikos.athanasop@gmail.com.

² Professor, Department of Mechanical Engineering & Aeronautics, University of Patras, 26500 Patras, Greece, siakavel@mech.upatras.gr.

I. Introduction

ALL satellites and the subsystems require the implementation of thermal control systems, materials, and strategies. Owing to the variable heat inputs, different strategies, devices, and materials are necessary for the thermal control. The most common design approaches for satellite thermal control involve coatings, heavy louvers (3 and 12 kg/m²) with a total emissivity ratio of 6–8, radiators connected to the satellite through heat pipes, heaters, thermostats, and controllers^{1,2}.

Moreover, shape memory alloys (SMAs) play a primary role in the development of systems capable of handling the thermal radiation. Reversible thermal panel (RTP) radiators alter their function from a radiator to a solar absorber in order to save power. RTP radiators use a high thermally conductive graphite sheet in order to transfer the heat to the deployable flat panel, and an SMA acts as an actuator in order to close or open the panel^{3,4}. Similarly, highly conductive carbon fiber reinforced plastic (CFRP) radiators that deform their geometry via SMAs to expose a material with high emissivity have been developed and tested⁵. Smaller shape memory structures of a few centimeters allow or prevent the energy exchange with the environment⁶.

As the volume of a satellite decreases, most of the aforementioned systems cannot be used owing to their high weight, volume, complexity, and energy demands. To boost smaller satellites, engineers in NASA have re-established the classic louver technology by reducing louver dimensions in order to fit them into nano-satellites⁷. Moreover, extremely complex micro-electromechanical devices (MEMs) that incorporate hinges and actuators can actively control the absorption/rejection of thermal radiation for space applications using high-voltage power supplies (micro-louvers), and act as variable emissivity surface (VES). The micro-scaled louvers can be attached to a radiator as a VES, thus achieving a fivefold change in their effective thermal emissivity^{8,9}. On the other hand, micro-louvered surfaces present several disadvantages. The performance of the micro-louvers has remained at low levels due to their extensive micro-patterning, complexity, and the use of high-voltage power supplies. Another promising thermal control solution is the use of electrochromic materials¹⁰. Moreover, it has been shown that materials with temperature-dependent thermo-optical properties can alter their infrared (IR) emissivity from low to high as the temperature increases from 173 K to 375 K¹¹ and from high to low; such a material is VO₂¹².

All aforementioned approaches suffer from major drawbacks: the devices are extremely complex and heavyweight; MEMs are heavy, extremely complex, and high-cost; certain materials either require power supplies or are incapable of becoming activated at various temperature ranges.

More versatile design strategies are required in order to a) decrease the temperature fluctuations and the thermal fatigue, b) reduce or eliminate the energy consumption of the electrical heater, and c) reduce the weight and the cost of the thermal control systems (TCS). Ultralight smart surfaces with variable emissivity have been proposed and tested by the present authors¹³⁻¹⁵. The smart surfaces are able to manipulate thermal radiation passively, without the use of controllers, sensors, and power supplies. These smart surfaces consist of smaller unit cells and respond passively to temperature and thermal radiation, Fig. 1.

Using these smart surfaces, it is possible to design the entire emissivity curve as a function of temperature, as well as to drastically modify the thermal emissivity / absorptivity / reflectivity / transmissivity of a surface through the combination of different coatings and the orientation of the unit cells¹³. When the unit cells are in the closed position, the effective emissivity is small. As the temperature increases, the unit cells open and the effective emissivity increases owing to the internal high-emissivity coating, thus creating a variable behavior as a function of temperature. Their designed behavior can be achieved through the prediction of their shape transformation by regulating the view factor of the

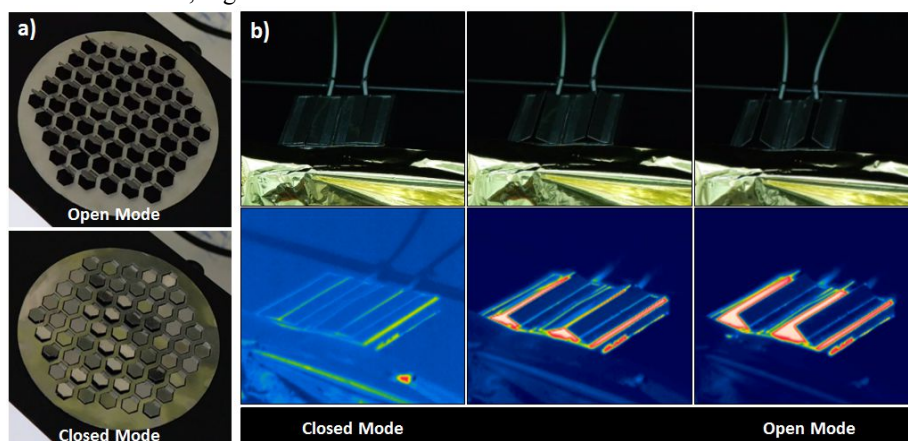


Figure 1. Different manufactured smart surfaces. a) Smart surface with hexagonal unit cells, a) Smart surface with rectangular unit cells and their thermographic images in different temperatures.

self-folding unit cells and of the material (coating) that is exposed to the environment, thus creating a surface with variable thermal radiation properties. The temperature-dependent effective thermo-optical properties could follow desired linear or non-linear profiles and achieve the desired absorptivity / emissivity ratios as a function of temperature¹³. These arrays transform their shape via developed internal stresses, which are due to the large mismatch of the coefficient of thermal expansion (CTE) of the multilayer material, and can perform very complex movements with large displacements and rotations. Isotropic materials can perform only bending movements, whereas anisotropic materials can be designed to perform twisting and combined modes. Their behavior is similar to that of “4D biomimetic materials”^{16,17}.

In this paper, our scope is to study and develop ultralight patterned surfaces of variable emissivity with high $\Delta\varepsilon$ in small ΔT . Moreover, we will provide critical information regarding their thermal fatigue resistance using low-cost experiments, and we will re-calculate the temperature of a certain CubeSat for the worst hot and cold case. We developed geometrically non-linear numerical models for two different types of smart surfaces in order to calculate the effective emissivity of each smart surface as a function of temperature. Then, we manufactured the smart surfaces and we measured the effective emissivity of the most promising design as a function of temperature. Moreover, we conducted low-cost and out-of-vacuum thermal fatigue tests to measure the shape-shift of the unit cells—which can be caused by the thermal degradation of the material properties—and to highlight the problems that may emerge. Finally, the predicted emissivity functions were used for the preliminary thermal re-design of a certain nano-satellite for the worst hot- and cold-cases by using simplified steady-state energy balance equations.

II. Design of the Smart Surfaces and Calculation of the Variable Emissivity Function

A. Materials and designs of the smart surfaces

The smart surfaces have an overall area of ($A = 100 \text{ cm}^2$) and can be tiled using a combination of unit cells. We developed and studied theoretically two smart surfaces ($10 \text{ cm} \times 10 \text{ cm}$), the unit cells of which had different geometrical characteristics (Fig. 2). The smart surfaces consisted of an array of 15 unit cells (Figs 2a–c) and 21 unit cells (Figs 2d–e), respectively. Each unit cell consists of a non-deformable region, a deformable region, and stiffeners (Figs 3). The deformable regions are very responsive to temperature, presenting extremely large deformations. The mismatch of the coefficient of thermal expansion (CTE) between the various layers creates a multilayer material that is very sensitive to temperature and alters its shape drastically owing to the developed internal stresses and their anisotropic nature. The sequence of the layers and the materials of the non-deformable and deformable regions that were used for the development of various patterned surfaces are presented in Fig. 3.

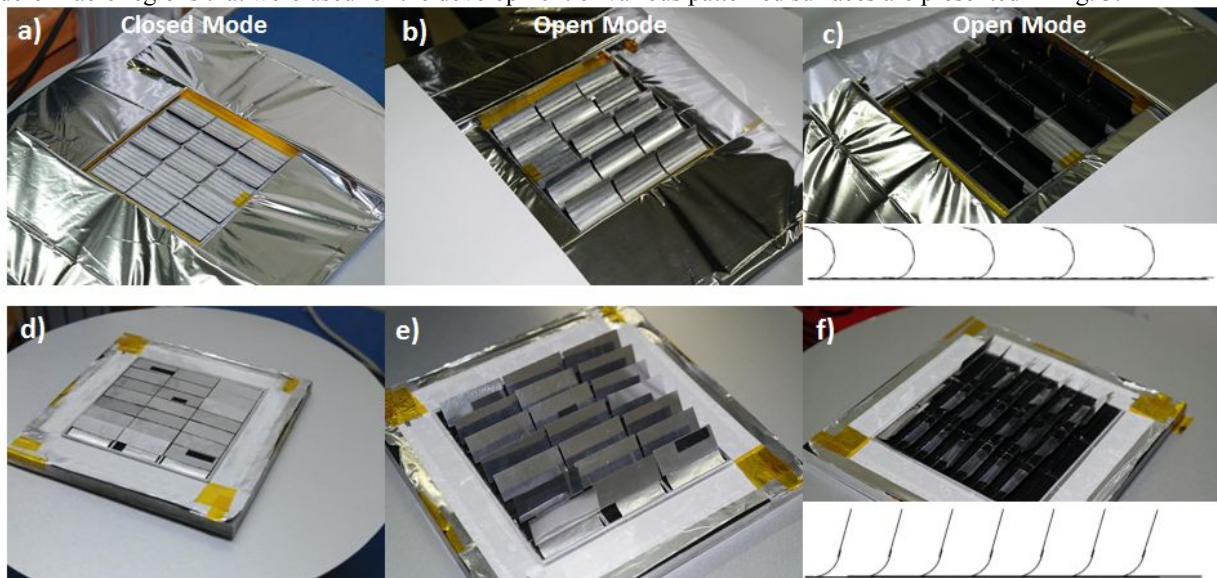


Figure 2. Developed smart surfaces ($10 \text{ cm} \times 10 \text{ cm}$). a-c) Smart surface with the 1st type of unit cells, d-e) Smart surface with the 2nd type of unit cells. The detail at the right dictates the unit cells that have been modeled using COMSOL software.

When the unit cells are in the closed position (Figs 2a and 2d), the effective emissivity is low. As the temperature increases, the unit cells open (Figs 2b and 2e) and the effective emissivity increases owing to the internal high-emissivity paint / coating (Figs 2c and 2f), thus creating a variable behavior as a function of

temperature. The position of the unit cells reaches a steady state at certain temperature levels. Above or below these temperature levels, the unit cells cannot be transformed further and the effective emissivity remains constant.

1. 1st Design of the smart surface

Each unit cell of the first design approach can be deformed entirely, Fig. 3a. Stiffeners of thick aluminum layers were formed in a few regions to increase the durability of each unit cell. Moreover, at the tip of the unit cells, one more layer of aluminum was placed in order to cover the gap between the two unit cells and to minimize the lowest value of the thermal emissivity of the smart surface. The thickness of the multilayer material is 0.11 mm, whereas the thickness of the non-deformable regions is 0.35 mm. The total weight of a 100 cm² smart surface is 3.3 gr, which ultimately leads to a weight of 330 gr/m².

2. 2nd Design of the smart surface

The unit cell of the second design can be deformed partially. In this case, a portion of the length of the unit cell is deformable. A larger stiffener (non-deformable region) has been designed to cover the deformable region of the next unit cell (Fig. 3b). Using this design we can make the unit cell more sensitive to temperature because the length of the deformable region is greater than that of the 1st design. However, the overall weight of a 100 cm² the smart surface is 7.3 gr. In this case, the areal weight is 730 gr/m². The areal weight of the 2nd design is 2.21 times heavier than that of the 1st design.

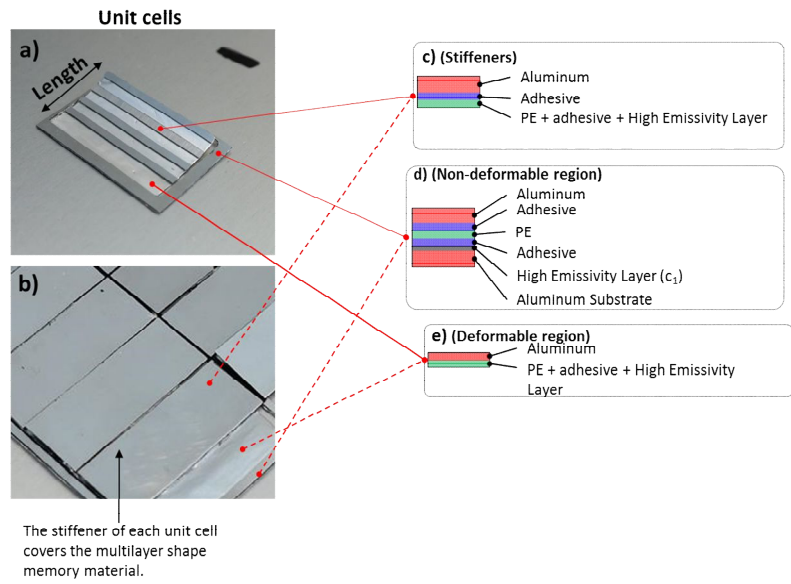


Figure 3. Developed unit cells and stacking of the multilayer materials of the different regions. a) 1st design, b) 2nd design, c) Multilayer materials in the stiffener region, d) Multilayer material of the supported regions and e) stacking of the active multilayer material (Aluminum, Oriented polyethylene-PE and adhesive).

B. Numerical models and calculation of the effective emissivity as a function of temperature

1. Numerical modelling

The smart surfaces were designed and modelled as plain-strain, geometrically non-linear problems. A heat flux (Q) was set below the smart surface; all unit cells and the interaction with one another were modelled as well. The steady-state temperature field of the smart surfaces was calculated for different heat flux values; therefore, the effective emissivity could be calculated as a function of temperature.

The non-linear behavior of the problem originates from the geometrical non-linearity that is due to the small thickness and the large displacements of the multilayer material¹⁸, and not the properties of the material. In our case, it is necessary to solve a coupled thermo-mechanical and geometrically non-linear problem, which would also incorporate the interactions of the body due to the thermal radiation. The strains are represented by the Green–Lagrange strain tensor; the stresses are represented by the Second Piola–Kirchoff stress tensor. Structured quadrilateral elements were used to model the overall phenomenon, taking into consideration the geometrical nonlinearities. In this case, the nonlinear terms and the cross derivatives exist, allowing the large deformation of elements as a function of temperature.

$$e_{el} = \frac{1}{2} [(\nabla u)^T + \nabla u + (\nabla u)^T \nabla u] - a(T - T_{ref}) \quad (1)$$

The radiosity leaving a surface is defined by Eq. (2):

$$J_i = \rho_i G_i + \varepsilon_i \sigma T_i^4 \quad (2)$$

where (ρ_i) and (ε_i) are the surface reflectivity and emissivity, respectively; (i) denotes the surface of the low- or the high-emissivity material. In general, the irradiation, (G), of the surface can be written as a sum:

$$G_i = G_{m,i} + F_{a,i} \sigma T_a^4 \quad (3)$$

where (G_m) is the mutual irradiation coming from other boundaries, (F_a) is an ambient view factor, and (T_a) is the assumed far-away temperature in the directions included in (F_a). In fact, (G_m) is the integral over all visible points of a differential view factor, (F), times the radiosity, (J), of the corresponding source point. In the discrete model, (G_m) may be expressed as the product of a view factor matrix and a radiosity vector. By inserting Eq. (3) for (G) to Eq. (2), the following equation is obtained:

$$J_i = \rho_i [G_{m,i}(J) + F_{a,i} \sigma T_a^4] + \varepsilon_i \sigma T_i^4 \quad (4)$$

Assuming an ideal gray body, Eq. (4) becomes

$$J_i = (1 - \varepsilon_i) [G_{m,i}(J) + F_{a,i} \sigma T_a^4] + \varepsilon_i \sigma T_i^4, \quad i = 1, 2, \dots, N \quad (5)$$

Equation (5) results in an equation system in (J) that is solved in parallel with the equation for the temperature, (T); (N) expresses the number of surfaces of which the overall structure consists. All the developed models have the same thermo-optical properties. On the internal surfaces of the unit cells, the emissivity is high ($\varepsilon_1 \approx 0.95$), and on the external surface of the unit cells the emissivity is low ($\varepsilon_2 \approx 0.075$).

Figures 4a and 4b present the meshed smart surfaces and the details of the meshing of the 1st design and 2nd design, respectively, in open and closed modes. The heat flux (Q) is applied at the bottom of the surface.

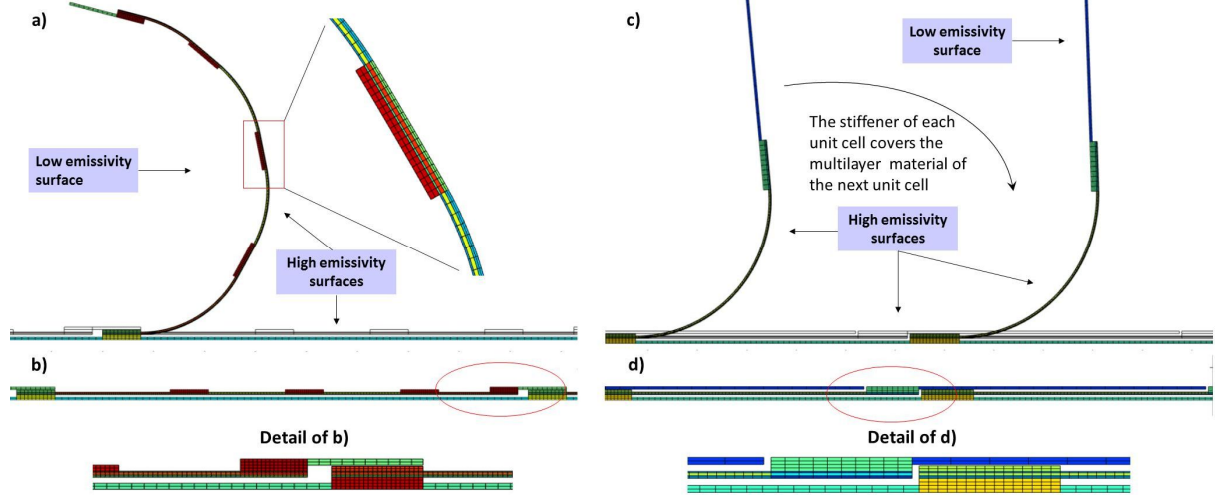


Figure 4. Representation of the unit cells of the smart surfaces during transformation using COMSOL Software, and details of the meshing grid. a) One of the open unit cells at steady state at 50 °C and b) at closed state, c) One of the open unit cells at steady state at 50 °C and d) at closed state.

2. Calculation of the effective emissivity

The prediction of the transformed geometry of the unit cells and the temperature field for various heat fluxes allow us to calculate the effective emissivity, Eq. (6). For each steady-state position and temperature field, the effective emissivity can be calculated as follows:

$$\varepsilon_{eff} = Q / \sigma(T^4 - T_\infty^4) \quad (6)$$

where Q is the heat flux, T is the temperature, and σ is the Stefan–Boltzmann constant.

Figure 5a presents the calculated emissivity of the two different designs of smart surfaces as a function of temperature; it illustrates that the emissivity curve of the 2nd design is slightly more sensitive to the temperature change. The minimum emissivity value was programmed to be reached at 5 °C in both cases. Below 5 °C, the emissivity remains constant for both designs. The effective emissivity curve of the 2nd design (black line) appears to be more sensitive to temperature changes because the stiffener (thick aluminum region) covers a larger area and the temperature gradient along the length of the unit cell is smaller. Moreover, the tip of each unit cell remains straight as the temperature increases, and does not cover the area that is located behind the unit cell. Despite the fact that the

second smart surface appears to be more efficient, a major drawback may be observed. The weight of the 2nd design is 2.21 times higher than that of the 1st design. Moreover, its structure is more complex. For this reason, we studied further the 1st design in terms of geometrical characteristics and material properties.

The emissivity of the 1st smart surface design changes its value from 0.1 to 0.83 ($\Delta\varepsilon = 0.73$) within a temperature change of $\Delta T = 36$ °C, and from 0.1 to 0.92 ($\Delta\varepsilon = 0.82$) within a temperature change of $\Delta T = 49$ °C (blue line, Fig. 5a). In this case, the total length of the unit cell is equal to $L = 18$ mm.

By setting the minimum emissivity value at 13 °C, the emissivity curve shifts (dotted black line, Fig. 5b). In Fig. 4b, we presented the effective emissivity as a function of temperature for the 1st type of unit cell for two different unit cell lengths and moduli of elasticity. For values of the modulus of elasticity, and CTE that are closer to more realistic values, the emissivity curve becomes less sensitive to the temperature (solid black line, Fig. 5b) and the emissivity change from 0.1 to 0.865 within $\Delta T = 56.7$ °C.

A unit cell with a length of 18 mm leads to an emissivity change from 0.1 to 0.865 within $\Delta T = 56.7$ °C (black solid line, Fig. 5b), whereas a unit cell of a length of 22 mm and the same elasticity modulus leads to an emissivity change from 0.1 to 0.86 within 43.6 °C (red solid line, Fig. 5b).

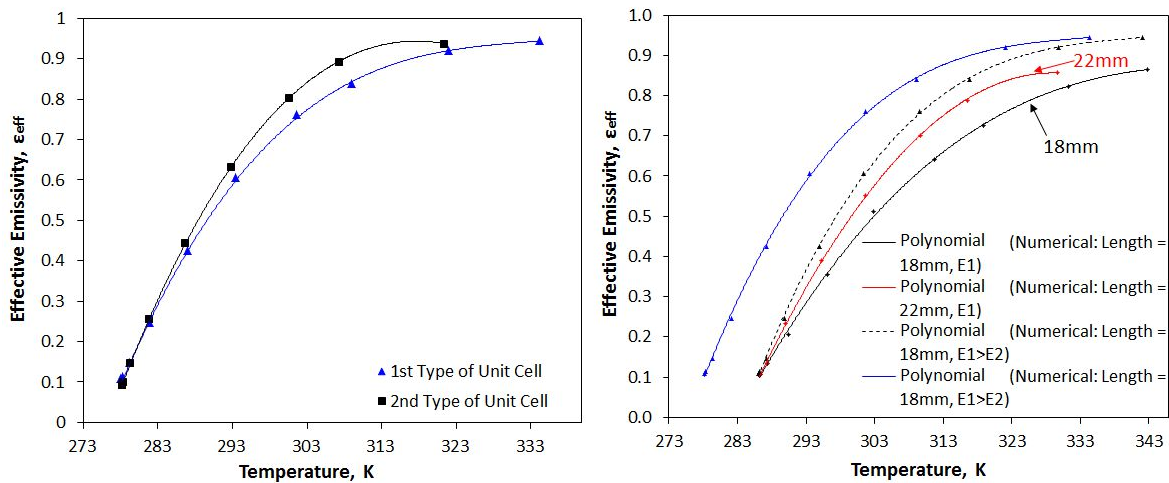


Figure 5. a) Calculated effective emissivity of the two different smart surface designs (closed state at 5 °C), b) Calculated effective emissivity of the 1st smart surface design with different material properties and geometrical characteristics.

III. Experimental Verification of the Effective Emissivity of the Smart Surfaces Using Calorimetric Measurements

The effective emissivity of two smart surfaces, which are based on the first design, was measured for different temperature levels using a comparative calorimetric method. On the internal surfaces of the unit cells, the emissivity is high ($\varepsilon_1 \approx 0.95$), and on the external surface of the unit cells the emissivity is low ($\varepsilon_2 \approx 0.075$).

A. Experimental apparatus and methodology

We employed a comparative calorimetric method under vacuum to measure the effective emissivity of the smart surfaces. We placed a few layers of black matte paint ($\varepsilon_{black} \approx 0.93-0.95$) on the surface of an aluminum thermal pad, which was then placed into the vacuum chamber. A silicon heater pad (12 W) was used in order to heat up the temperature aluminum panel. We connected the silicon heater pad with a direct current (DC) voltage power supply. Voltage was applied to the thermal pad resulting in a uniform temperature increase on the surface. We attached the upper side of the heater pad to the bottom of the aluminum flat plate, which had a thickness of of a 2 mm. The opposite side of the pad was covered with an aluminum plate. We attached a pure highly polished silver sheet with a thickness of 0.3 mm to the lower and to the external surface of the aluminum thermal pad to prevent heat transfer via radiation as much as possible. We measured the steady-state temperature of the aluminum surface as a function of the applied power at a certain medium vacuum level (12 ± 0.2 Pa) and at constant temperature of the chamber walls (T_∞). The vacuum and the outer temperature remained constant for 200 min prior to starting each experiment. For each temperature level ($T_1 \approx 25$ °C, 30 °C, 40 °C, 50 °C, 55 °C and 60 °C), the steady-state temperature was maintained for at least 30 min to ensure that there would be no temperature change versus time ($T = T_{Steady-state} \pm 0.01$ °C). Two thin K-thermocouples specially designed for vacuum measurements were placed inside the aluminum plate

at a distance of 0.1 mm below the black paint. We used a stabilised DC power supply (TTi QPX1200SP Bench Power Supply) to accurately regulate the voltage (accuracy Voltage-resolution Voltage - 1 mV). We measured the applied voltage with a multimeter (GW Instec, GDM-8251A), with an accuracy of $\pm(0.012\% \text{ rdg} + 5 \text{ digits})$. The current was measured with accuracy of $\pm 100 \mu\text{A}$.

While maintaining all aforementioned parameters constant, we placed the smart patterned surface on the aluminum thermal pad and inside the vacuum chamber; we then identified the required applied power for each aforementioned temperature level. The effective emissivity was determined as a function of temperature through the following equation.

$$Q_{black}^{electrical} \Big|_T - Q_{black}^{rad} = Q_{smart}^{electrical} \Big|_T - Q_{smart}^{rad} \Rightarrow \epsilon_{eff}^{smart} = \frac{VI^{smart} - VI^{black} + \epsilon_{black} \sigma A (T^4 - T_{\infty}^4)_{black}}{\sigma A (T^4 - T_{\infty}^4)_{smart}} \quad (7)$$

We recorded and compared the measurements of (T, T_{∞}, V, I) for each effective emissivity value with those of the black coating. It is highly important that $(T^4 - T_{\infty}^4)_{black} \approx (T^4 - T_{\infty}^4)_{smart}$ between the two comparative measurements.

Additionally, we recorded and compared the resistance of the overall circuit with the previous measurements to avoid uncertainties and potential internal faults. We continuously recorded the temperature of the inner black matte surface of the vacuum chamber (T_{∞}) using an array of six thermocouples. The thermocouple arrays measured the temperature of the internal wall of the vacuum chamber (0.1 mm above the internal thick black surface). The measurements were continuously recorded with a 500 ms sampling rate, and stored in a PC via a calibrated USB data acquisition hardware (Picolog). All measurements were obtained once steady-state conditions were reached. To avoid measurement discrepancies, we used a steel vacuum chamber; we coated all inner-wall surfaces with three layers of black matte paint, with an emissivity of approximately $\epsilon \approx 0.95$, to create a large black-body cavity and to ensure that the reflections would be negligible. We realized this black-body effect by employing a highly absorbing surface, by making the surface area considerably larger than that of the specimen, and by avoiding any external energy radiation sources. The thermal pad and the investigated materials were located near the centre of the vacuum chamber. The temperature uniformity over the heater pad ensured that the entire surface would radiate energy uniformly. An IR camera (FLIR SC660) was used in order to check the temperature uniformity of the aluminum thermal pad—outside the vacuum chamber—while the temperature deviation between the two thermocouples was negligible for all cases.

B. Measurement of the effective emissivity as a function of temperature

The effective emissivity of two smart surfaces, which were based on the first design, was measured for different temperature levels. The unit cells of the first measured smart surface had a length of 18 mm, whereas the length of the second surface was 22 mm.

By observing the emissivity difference between the theoretical and experimental results, we may conclude that the theoretical results are in good agreement with the experimental measurements (Fig. 6). Both cases presented a high emissivity change.

In Fig. 6, the solid black dots represent the emissivity of the high-emissivity coating, whereas the blue crosses and black asterisks represent the emissivity of aluminium and of a 100% silver foil, respectively. The emissivity measurements of different materials were obtained in

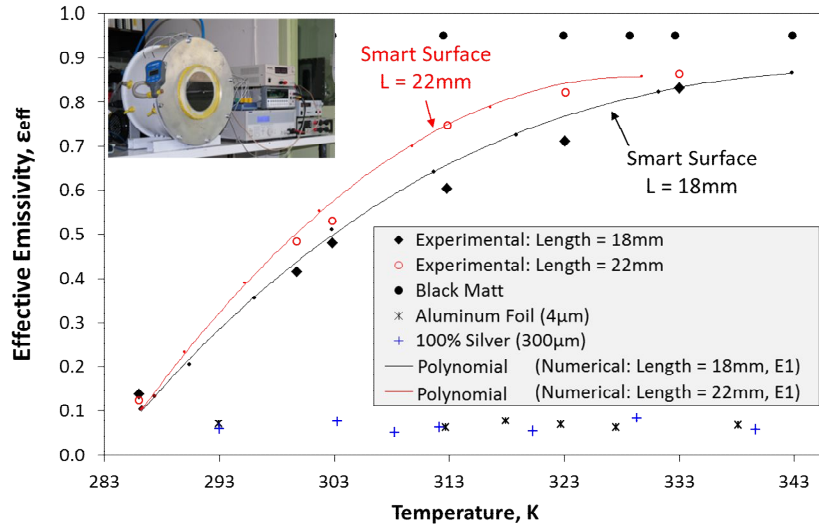


Figure 6. Measured effective emissivity as a function of temperature versus theoretically predicted values for two smart surfaces with different unit cells.

order to develop benchmark experiments and to ensure that the apparatus and the measurement methodology are accurate.

The 1st tested surface (unit cell length of 18 mm) leads to an emissivity change of $\Delta\varepsilon = 0.572$ (0.138 to 0.71) within a temperature change of $\Delta T = 37.1$ °C (black solid diamonds, Fig. 6), whereas the emissivity change of the second tested surface (unit cell length of 22 mm) leads to a $\Delta\varepsilon = 0.70$ within a temperature change of $\Delta T = 37.1$ °C (red circles, Fig. 6). Moreover, for a temperature change of $\Delta T = 47$ °C, the emissivity change of the first and the second smart surface is $\Delta\varepsilon = 0.694$ and $\Delta\varepsilon = 0.737$, respectively. Small differentiations in the behaviour of the acquired and the theoretical curves may be present owing to the specular nature of the aluminium surface, as well as the inequality of the absorptivity and the emissivity of the external aluminium surface, $\alpha_{al} > \varepsilon_{al}$. Moreover, small non-homogeneous regions in the multilayer material may lead to small deviations in the deformation of the unit cells.

IV. Degradation of the Material Properties and Resistance to Thermal Fatigue

We studied the response of the transformable unit cells and how their geometry was affected by the degradation of the mechanical properties of the multilayer material under different thermal conditions. In the first test, we investigated the change in the geometry of a unit cell at a steady-state temperature for a period of 720 h (1 month). In the second test, we studied the changes in the geometry of a unit cell under fast and out-of-vacuum thermal fatigue conditions. Finally, we investigated whether the thermal fatigue would significantly affect and locally degrade the multilayer material and the performance of the smart surfaces. Through the aforementioned low-cost experimental methodologies, we intended to examine the performance of the smart surfaces and to identify potential problems prior to proceeding to more laborious and expensive tests.

A. Degradation of the unit cells for short-term thermal aging

A short-term thermal aging test was conducted in order to study the degradation of the multilayer material and consequently the shape-shift of the unit cell after 720h at 50°C. Any shape-shift of the unit cell will alter the minimum and maximum emissivity values and the performance of the smart surface will be reduced.

A unit cell was placed in an insulated small temperature controlled apparatus. The unit cell was designed to be in closed state at 13°C and was heated-up until the maximum set temperature (50 ± 0.5 °C). Two thermal pads and a fan were used in order to heat-up uniformly the chamber. A thick aluminum honeycomb was placed between the fan and the specimen in order to minimize any disruption of movement of the unit cell by the air (Fig. 7b). The controller was set to keep the temperature between 49.5°C and 50.5°C. Three thermocouples were placed near the specimen in order to continuously record the temperature and ensure the temperature uniformity.

During the heating stage, the smart material transformed to its final shape. A laser distance meter (micro-epsilon, CS3) recorded the position of a certain point of the unit cell every 10 s during the transformation of the multilayer material at the maximum controlled temperature. The total duration of the experiment was 1 month; during this period, the temperature of the chamber was allowed to revert to the environmental temperature 9 times. Any change in the final position of the measured point was indicative of the fact that the mechanical properties of the multilayer material were degraded and that the shape of the unit cell changed, Fig. 7.

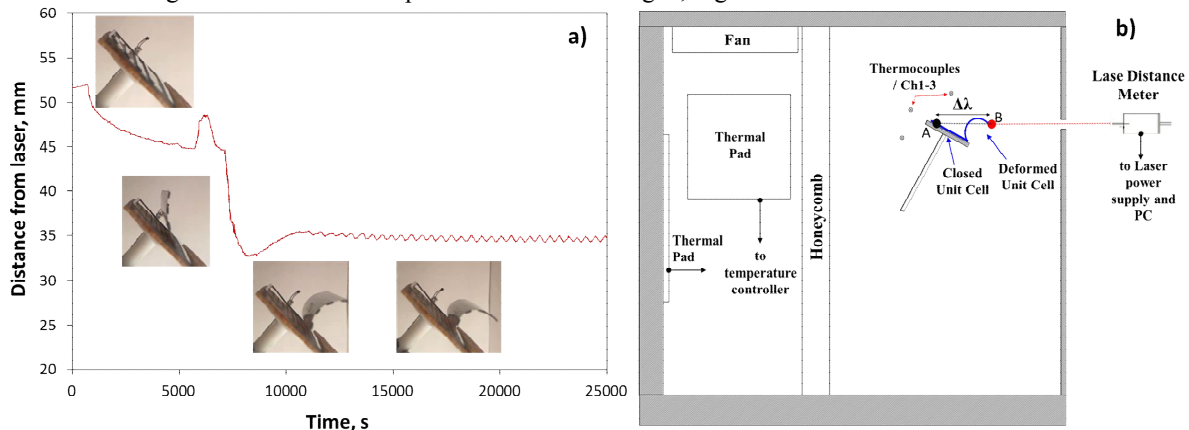


Figure 7. a) Recorded distance of the position of the measurement point A to B as a function of time during the heating stage and b) Schematic representation of the chamber.

Figure 7a presents the recorded distance between the laser device and the measured point, as well as the transformation of the unit cell until it reached its final position (from point A to point B, Fig. 7b). The first peak is caused by the stiffener. The second lower peak of the red curve is caused by the fact that after a 2 °C increase the laser measurement point is no longer on the edge; it is on the internal surface.

In Figure 8, we may observe that after 750 h at a maximum temperature of 50.5 °C, the measured point at the final transformed shape has been altered by 1.05 mm. Despite this small change, we may observe that this value becomes stabilized to a value that does not change any further. This small shape-shift dictates that the polyethylene and the adhesive layers became harder. On the other hand, the initial position (closed state of the unit cell) after 750 h was altered only for $\Delta\lambda_0 - \Delta\lambda_{750h} = 0.54$ mm (from $\Delta\lambda_0 = 51.88$ mm to $\Delta\lambda_{750h} = 51.34$ mm). In this case, the closed state of the unit cell is shifted from the 13 °C approximately to 11.5 °C. Moreover, we may observe that the transformation of the unit cell between 49.5 °C and 50.5 °C deviated between 35.8 mm and 36.2 mm (detailed diagrams in Fig.8). The sensitivity of the multilayer material is profound, and any shape-shift due to the thermal degradation can be considered during the design of the material.

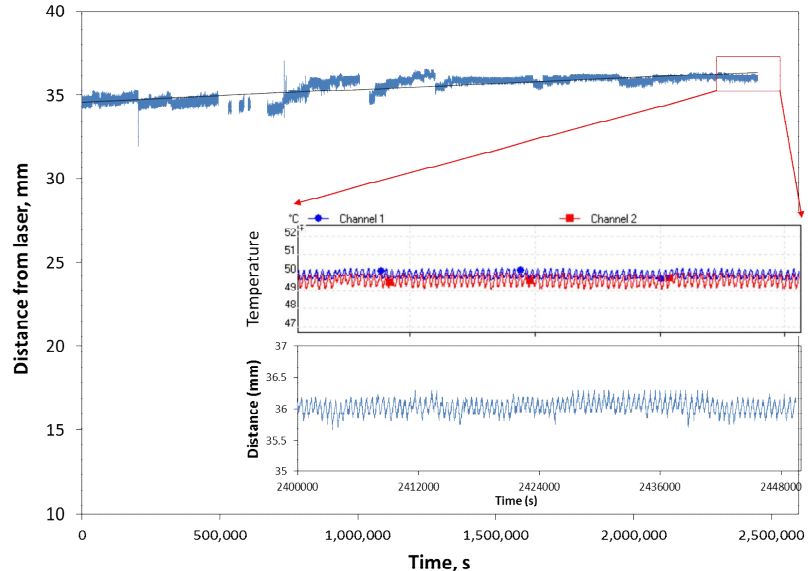


Figure 8. Identification and measurement of shape-shifting during the short-term thermal aging test at the maximum operational temperature.

B. Fast and out-of-vacuum thermal fatigue of unit cells

A setup was developed to study the degradation of the mechanical properties of the multilayer material and the shape-shifting of the unit cell. As the temperature changed, the transformation of the geometry of the unit cell was related to the mechanical properties of the different layers. During the transformation of the unit cell any degradation / change in the polymeric layers would result to a different shape. Moreover, any failure of the layers or any interlaminar failure would result to the shape shift of the unit cell.

The scope of this experimental procedure is to evaluate the material performance of the unit cell under accelerated thermal fatigue. In the future, these preparatory tests will guide us to examine the durability of the unit cell under a thermal fatigue load using more sophisticated, laborious, and combined experiments, such as a) thermal fatigue under vacuum or b) thermal fatigue under vacuum and VUV / UVC radiation.

The experimental setup consisted of an IR lamp, a fan, a digital timer and counter, a power supply, a laser distance meter (micro-epsilon CS3), a reflector curtain, and the tested unit cell, Fig. 9b. The digital timer controlled the operation time of the IR lamp and that of the fan. The IR lamp heated the unit cell until it reached its final-transformation position at 50–52 °C. Immediately after the heating phase, the unit cell was cooled using a fan as a cooler and it returned to its initial position. The duration of each thermal cycle was 15 s (6 s for the heating phase and 9 s for the cooling phase), leading to a total of 240 thermal cycles per hour. A laser measurement device was continuously recording the distance of a constant point (from A to B, Fig. 9b) during the cooling phase. Any change in the recorded distance during cooling or any change in the measured distance of the initial position (A) or final position (b) would indicate that the mechanical properties of the multilayer material have been degraded or that a failure has occurred.

Figure 9a presents the measured distance versus time at the cooling phase after a certain number of thermal cycles. The black line presents the average value of the measured distance of 10 thermal cycles after 1,000 thermal cycles ($(N_{1000}-N_{1010})/10$) versus time, whereas the red and blue lines present the average value of the distance of ten

thermal cycles after 50,000 thermal cycles $(N_{50000}-N_{50010})/10$ and 78,000 thermal cycles $(N_{78000}-N_{78010})/10$, respectively.

The distance between the location of the initial position (Point A, Fig. 9b) at the beginning of the test and at the end of the test after 78,000 thermal cycles changed by 1 mm, whereas the distance between the location of the final position (Point B, Fig. 9b) during the beginning and the end of the test changed by 0.9 mm. Essentially, the shape of the multilayer material alters slightly creating a convex shape.

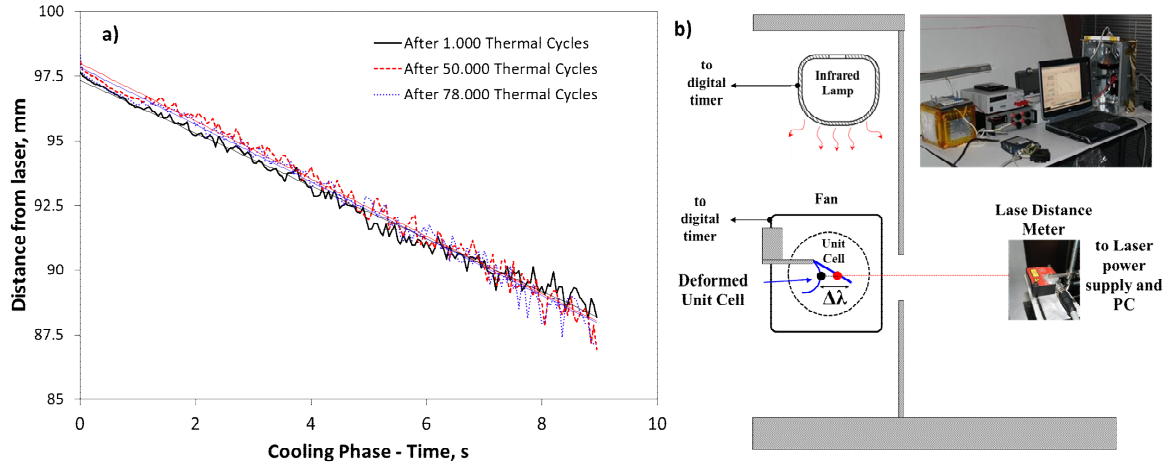


Figure 9. a) Distance measurement of the position of point A to point B during the cooling stage after 1,000, 50,000 and 78,000 thermal cycles, b) Apparatus of the thermal fatigue test.

The multilayer material was more rigid and its response to temperature was less sensitive. Due to this hardening of the polymeric layers, the effective emissivity of the smart surface after 78,000 thermal cycles will be different and lower than the effective emissivity at the beginning of life (BOL). The hardening of the material is also related to the heating and cooling rate; therefore, smaller rates would lead to smaller shape shifts because of the materials degradation at the end of life (EOL). The tested unit cells after 78,000 thermal cycles were still healthy and no failure was present.

C. Thermal fatigue for the identification of local failures

A smart surface was tiled by small hexagonal unit cells with the purpose of examining potentially defective regions of the multilayer material. The smart surface was tested using the same experimental setup for 132,000 thermal cycles. The duration of each thermal cycle was 100 s (60 s for the heating phase and 40 s for the cooling phase) for 38,000 thermal cycles, leading to 36 thermal cycles per hour. After 38,000 cycles, the duration was set to 20 s per thermal cycle (18 s for the heating phase and 12 s for the cooling phase) for 94,000 thermal cycles, leading to 120 thermal cycles per hour.

Despite the very good performance of the multilayer material, we observed that local degradation may occur because of material imperfections and inaccuracies in the manufacturing process.

Figure 10 illustrates that three (3) unit cells are unable to respond after 132,000 thermal cycles with the increase in temperature. The maximum temperature during the entire thermal fatigue testing was approximately $\approx 80^\circ\text{C}$.

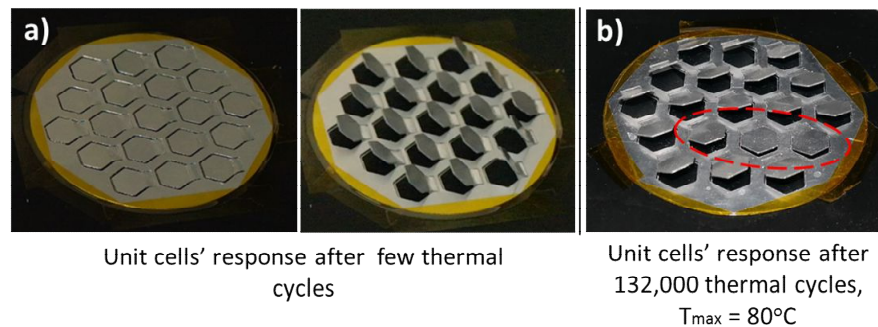


Figure 10. Thermal fatigue of a patterned surface for the identification of local failures. a) Healthy material at the closed and open state. B) Smart surface after 132,000 thermal cycles, $T_{\max} = 80^\circ\text{C}$.

V. Preliminary Thermal Re-design of a Nano-satellite

A. Worst hot and cold case using common materials from the COMPASS-1 team Scenario 1 (Benchmark)

A certain nano-satellite was selected in order to re-calculate the worst hot and cold case using the smart surfaces. The worst hot- and cold-case values were compared with the calculations of the COMPASS-1 team, which used common surface-finishing materials. The orbit of the COMPASS 1 is a circular, synchronous, near-sun low-Earth orbit (LEO) at an altitude of 600 km and an inclination of 98°. COMPASS 1 completes one orbital revolution in 96.30 min. For 60.52 min, the nano-satellite is exposed to sunshine, whereas for 35.38 min it is exposed to the Earth's shadow, thus cooling down^{19,20}. The high frequency at which COMPASS 1 rotates around the Earth (15 revolutions per day) causes extensive thermal fatigue, which results in the degradation of the structure, the adhesives, and of other parts. The application and the combination of different coatings and materials on the external surfaces of the nano-satellite control the equivalent emissivity and absorptivity of each side of the nano-satellite. Solar panels have high emissivity values and occupy most of the external surfaces of the nano-satellite.

Because of these reasons, the thermal energy is radiated into deep space during the eclipse and the temperature of the worst cold case is very low. By covering the empty areas of the nano-satellite's sides with the appropriate materials / coatings / paints, we can minimize the power of the heaters or eliminate the heaters.

During eclipse, nano-satellites rapidly reject energy into deep space and the solar cells receive no power. The batteries and the heaters start to function, and they control the temperature of the nano-satellite because passive thermal control cannot prevent overcooling. Increasing the minimum temperature of the nano-satellite would be ideal to reduce the emissivity of the outer surfaces during the eclipse and to increase the absorptivity. On the other hand, during the hot case, nano-satellites are in a constantly illuminated orbit, and the temperature increases rapidly owing to the high α / ϵ ratio of the external materials / coatings of the nano-satellite.

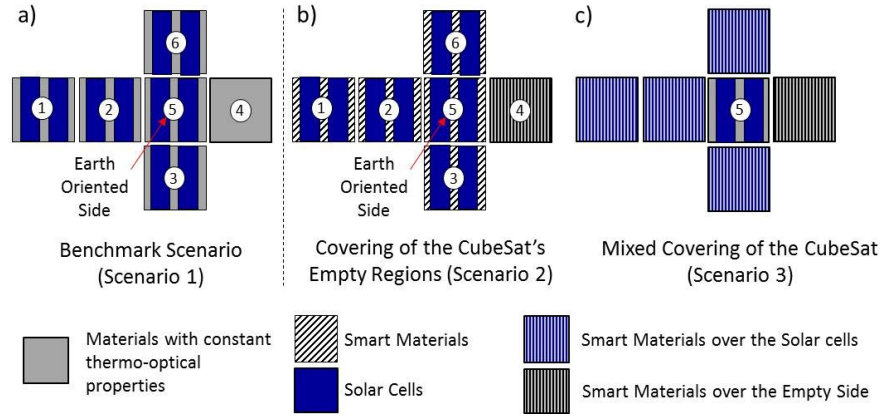


Figure 11. Different design scenarios. a) Sides 1-2-3-5-6 are covered 70% by solar cells and 30% by a material with constant thermo-optical properties. Side 4 is covered 100% by a material with constant thermo-optical properties^{19,20}, b) Sides 1-2-3-5-6 are covered 70% by solar cells and 30% by smart surfaces. Side 4 is covered by smart surfaces, c) The solar cells of Sides 1-2-3-6 are covered entirely by smart surfaces; Side 4 is covered by smart surfaces.

Different combinations of materials / coatings were studied by the COMPASS-1 team for the calculation of the hot and cold worst cases and for the identification of the best combination, Fig. 11a. The best combinations for the worst hot case is to cover 70% of Sides 1, 2, 3, 5, and 6 by solar cells and 30% by black paint, and to cover 100% of Side 4—which carries the antenna—by black paint. In this case, the maximum temperature would be $T_{\max} = 289.48$ K, if the Sun-oriented side has been covered by 70% solar cells and 30% black paint. The minimum calculated temperature in this case was $T_{\min} = 164.37$ K. On the other hand, the best combination regarding the worst cold case was achieved by covering Sides 1,2,3, and 6 with 70% solar cells and 30% aluminum and to cover 100% of Side 4—which carries the antenna—by aluminum and the Earth oriented side (Side 5) by 70% solar cells and 30% black paint. The minimum temperature was $T_{\min} = 182.74$ K, whereas the maximum temperature was $T_{\max} = 309.97$ K, where the Sun-oriented side has been covered by 70% solar cells and 30% aluminum^{19,20}. Moreover, the temperature deviation is $\Delta T \approx 127$ °C.

B. Preliminary design of the thermal control using the smart surfaces

A satellite during its orbit exchanges energy with several variable heat sources. The temperature of the nano-satellite varies owing to the cyclic alteration of the thermal loads during the orbit. For the preliminary thermal design, we calculated the worst hot and cold cases using the steady-state energy balance equation, Eq. (8) and making few simplifications in order to study the influence in the maximum and minimum temperature of a nano-satellite. In our calculations, we considered the nano-satellite as an one-node geometry. Subsequently, through the

energy balance equation, the developed minimum and maximum temperatures at the steady state can be calculated. The solar flux was ($I_S = 1370 \text{ W/m}^2$), the Earth IR was ($I_E = 250 \text{ W/m}^2$), whereas ($\dot{Q} = 1 \text{ W}$) was the internal heat dissipation—which is attributed to the solar cells, the wires, heaters, and the electronic components—(A) is the area of each side of the nano-satellite, ($T_{\text{Space}} = 3 \text{ K}$) is the deep-space temperature, and (T) is the average temperature of the nano-satellite.

For the worst hot case, the steady-state temperature can be calculated via the simplified equation, Eq. (8).

$$a_{S_s}(T)I_S A + 0.34a_{S_b}(T)I_S A + a_{IR}(T)I_E A + \dot{Q} = 5\varepsilon'_{IR}(T)\sigma A(T^4 - T_{\text{Space}}^4) + \varepsilon_{IR}(T)\sigma AT^4 \quad (8)$$

In the cold case, only the Earth's IR flux exists during the period of the maximum eclipse, without internal dissipation. The temperature of the cold worst-case scenario with zero internal energy dissipation at the steady state can be calculated via Eq. 9.

$$T^4 + \frac{\varepsilon_{IR}(T)T^4}{5\varepsilon'_{IR}(T)} = T_{\text{space}}^4 + \frac{I_E}{5\sigma} \frac{\alpha_{IR}(T)}{\varepsilon'_{IR}(T)} + \frac{\dot{Q}}{5\varepsilon'_{IR}(T)A\sigma} \quad (9)$$

In the case where the thermo-optical properties of the materials are constant, the aforementioned equations can be solved for (T_{max} and T_{min}). However, if the material properties are functions of temperature (e.g. $\varepsilon_{IR}(T)$), different numerical iterative methods can be used to extract the solutions. The thermo-optical properties of the smart surfaces are temperature-dependent variables. The energy balance equations cannot be solved directly owing to their complexity. To find the solution of each equation, the regula-falsi iterative method was used.

In this study, bounded equations (Eqs. (10) and (11)) were used in order to generate the emissivity and absorptivity curves of each side of the satellite. It has been proven that any curve can be generated using the proposed smart surfaces, and can be represented by the bounded curves¹³.

$$\varepsilon_{\text{eff}}(T) = \frac{\varepsilon_{\text{min}} - \varepsilon_{\text{max}}}{1 + e^{(T - T_{\text{mid}})/0.25\Delta T}} + \varepsilon_{\text{max}}, \quad (10)$$

$$\alpha_{\text{eff}}(T) = \frac{\alpha_{\text{min}} - \alpha_{\text{max}}}{1 + e^{(T - T_{\text{mid}})/0.25\Delta T}} + \alpha_{\text{max}}, \quad (11)$$

where the ε_{min} and ε_{max} values control the minimum emissivity and maximum absorptivity values, respectively; T_0 expresses the temperature at the middle of the curve, whereas ΔT controls the temperature level at which the emissivity changes. Moreover, T_0 along with ΔT can be designed to shift to any desired temperature value. When the smart surfaces are in the closed state, the radiation leakages were considered to be 1% (the validity of these assumption is related to the technologies that can be used for the manufacturing of the smart surfaces). The equivalent emissivity of each side of the nano-satellite can be calculated simply by averaging the thermo-optical properties of the materials in each side. E.g. if a side is covered 70% by solar cells and 30% by the smart surface, the equivalent emissivity and absorptivity of this side can be calculated simply via Eqs. (12) and (13).

$$\varepsilon_{\text{Side}}(T) = \varepsilon_{\text{eff}}(T) \frac{A_{\text{Smart}}}{A} + \varepsilon_{\text{Solar}} \frac{A_{\text{Solar}}}{A}, \quad (12)$$

$$\alpha_{\text{Side}}(T) = \alpha_{\text{eff}}(T) \frac{A_{\text{Smart}}}{A} + \alpha_{\text{Solar}} \frac{A_{\text{Solar}}}{A}, \quad (13)$$

where ($\varepsilon_{\text{side}}(T)$, $\alpha_{\text{side}}(T)$) are the equivalent emissivity and absorptivity of each side, (A_{Solar}) is the area of the solar cells, (A_{Smart}) is the area of the smart surface, (A) denotes the overall area of each side. Consequently, the average emissivity of the five sides that radiate into deep space can be calculated via Eq. (14).

$$\varepsilon'_{IR}(T) = \frac{4\varepsilon_{\text{Sides1,2,3,6}}(T) + \varepsilon_{\text{Side4}}(T)}{5} \quad (14)$$

Moreover, in this study we assumed that the values of the thermo-optical properties are in the BOL.

1. Application of the variable emissivity surfaces on 30% of the surface of each side – Scenario 2

We calculated the hot and cold worst-cases using the proposed smart surfaces, which covered only 30% of the area of each side and 100% of the area of the empty side of the nano-satellite, Fig. 11b. For all cases, the Earth-oriented side was covered by 70% Sc + 30% Smart surfaces (Sf). The smart surfaces were designed to open as the temperature increases. Different coating combinations (cases) were considered for the internal and external areas of

the smart surface. The aforementioned bounded equations were used in order to generate the different effective emissivity and absorptivity curves. The temperature range (ΔT) was set to 40 °C, and $T_0 = -8$ °C for all cases. Above and below the certain temperature range (ΔT), the equivalent values remain constant (ϵ_{\min} , ϵ_{\max}).

Case 1: The first case combines aluminum on the external areas of the smart surface ($\epsilon_{al} = 0.080$, $\alpha_{al} = 0.379$) and black paint on the internal areas of the smart surface ($\epsilon_{bp} = 0.900$, $\alpha_{pb} = 0.970$). These material properties were used in the aforementioned benchmark scenario.

Case 2: The second case combines silver on the external areas of the smart surfaces ($\epsilon_{p-sil} = 0.030$, $\alpha_{p-sil} = 0.090$) and martin black velvet paint on the internal areas of the smart surface ($\epsilon_{bv} = 0.940$, $\alpha_{bv} = 0.910$).

The results from the hot case calculations yielded the following results. The maximum developed temperature of the nano-satellite in the 1st case is $T_{\max} = 13.12$ °C (286.27 K) where the Sun-oriented side has been covered by 70% solar cells and 30% Smart surface. On the contrary, once more, the cold-case predictions yielded very low temperature levels $T_{\min} = -90.67$ °C (182.48 K) without internal dissipation. The temperature values for the cold worst-case rose by approximately 18 °C; however, this value is not a sufficient improvement for the overall temperature behavior of the satellite. Moreover, the temperature deviation drops from $\Delta T = 125$ °C (benchmark scenario) to $\Delta T = 103.78$ °C.

The maximum developed temperature of the nano-satellite in the 2nd case is $T_{\max} = 9.73$ °C (282.88 K) where the Sun-oriented side has been covered by 70% solar cells and 30% Smart surface. The minimum temperature is $T_{\min} = -88.55$ °C (184.60 K) without internal dissipation. The temperature deviation in this case is $\Delta T = 98.28$ °C.

Owing to these low temperature values, a heater would be needed. Despite the fact that ΔT decreased, the 30% of the area that was occupied by smart surfaces was not sufficient to drastically change the minimum temperature; the worst cold case is still not acceptable. We may conclude that the addition of only 30% of the smart surface over the empty sides of the nano-satellite is beneficial because the maximum temperature has decreased and the minimum temperature has increased for all cases.

2. Application of the smart surfaces on five sides of the nano-satellite – Scenario 3

The high emissivity of the solar panels rejected the thermal energy during the eclipse; thus, the nano-satellite became overcooled. Consequently, we studied an extreme scenario of covering a few solar panels* with smart surfaces due to the limitations of the empty areas (without solar cells), Fig. 11c. In this case, when the nano-satellite would exit the eclipse phase, the smart surfaces would open their unit cells, thus allowing the solar cells to absorb light. The smart surfaces can be programmed to completely open their unit cells within a small temperature change. It becomes obvious that the energy absorbed from the solar cells that is converted to electrical energy will be reduced. This is a matter of redesigning the electrical consumption, which will not be addressed in this study. On the other hand, by covering 100% of few solar panels with smart surfaces, we concluded that the power of the heater would be minimized or eliminated during the eclipse phase, and that the energy storage of the battery could be drastically reduced. In the 3rd scenario the Earth-oriented side (Side 5) was covered by 70% Solar cells + 30% martin black paint and all remaining sides were covered 100% by smart materials. In this case, the temperature change was $\Delta T = 39.51$ °C when the Sun-radiated side was covered by 100% smart surfaces. Moreover, the calculated minimum and maximum temperature were $T_{\min} = -25.01$ °C (248.14 K) and $T_{\max} = 14.5$ °C (287.65 K).

*This is a simplified scenario and we did not study in detail the overall behavior and the transient phenomenon.

VI. Conclusion

We drastically altered the emissivity value (approximately $\Delta\epsilon \approx 0.7$) within the temperature span of $\Delta T < 40$ °C; hence, we developed integrated, low-weight, cost-effective smart surfaces with variable emissivity. The material was developed to passively react over a very broad range of thermal requirements. Using these low-cost materials, we may passively control the temperature of the systems and sub-systems of a satellite through the regulation of the absorptivity/emissivity ratio, and we may reduce the weight and the complexity of the overall system. Moreover, we believe that the present work can significantly contribute to the future thermal design of various satellites/spacecraft for space exploration that are larger than nano-satellites. In addition, practically, we may design these materials to resist UV radiation or to absorb particular wavelengths. Due to the high thermal fatigue resistance, we conclude that further investigation is required and that thermal fatigue tests should be conducted using sophisticated and accelerated experiments under vacuum and VUV radiation. More detailed and transient models would allow more accurate predictions of the temperature during the mission, incorporating also the directional dependency of the absorptivity and emissivity of the smart surfaces.

Acknowledgments

This research is conducted through the IKY scholarships program, and is co-financed by the European Union (European Social Fund - ESF) and the Greek national funds through the action entitled “Reinforcement of Postdoctoral Researchers” of the National Strategic Reference Framework (NSRF), 2014–2020.

References

- ¹ Gilmore, D. G., *Spacecraft Thermal Control Handbook Volume I: Fundamental Technologies*, The Aerospace Corporation print, 2002.
- ² Furukawa, M., “Analytical Studies on Design Optimization of Movable Louvers for Space Use”, *Journal of Spacecraft and Rockets*, Vol. 16, No. 6, 1979, pp. 412 - 425.
- ³ Nagano, H., Ohnishi, A., and Nagasaka, Y., “Development of a lightweight deployable / stowable radiator for interplanetary exploration”. *Applied Thermal Engineering*. Vol. 31, 2011, pp. 3322–3331.
- ⁴ Nagano, H., Ohnishi, A., Nagasaka, Y., and Nagashima, A., “Study on a reversible thermal panel for spacecraft (detailed design based on parametric studies and experimental verification)”, *Heat Transfer—Asian Research*, Vol. 35, No. 7, 2006, pp. 464–481.
- ⁵ Cognata, T. J. et al. “A Morphing Radiator for High-Turndown Thermal Control of Crewed Space Exploration Vehicles”, *23rd AIAA/AHS Adaptive Structures Conference*, 1509, 2015.
- ⁶ Matovic, J., and Reichenberger, K., “Variable emissivity surfaces for micro and nanosatellites”, *ASME Proceedings | Systems and Sub-Systems*, Paper No. CANEUS2006-11027, pp. 135-140.
- ⁷ Willingham, A. L., “Cubesat form factor thermal control louvers”, Patent US20170088294A1, 2015.
- ⁸ Osiander, R., Firebaugh, S. L., Champion, J. L., Farrar, D. and Darrin, M. A. G., “Microelectromechanical devices for satellite thermal control”, *IEEE Sensors*, Vol. 4, 2004, pp. 525–531.
- ⁹ Cao, S. et al. Variable emissivity surfaces for micro and Nano-satellites. *Phys. Procedia* 18, 91–94 (2011).
- ¹⁰ Anderson, K., Zay, B., McQueeney, T., and Chandrasekher, P., “Electrochromic radiators for microspacecraft thermal control”, *19th Annual AIAA/USU Conference on Small Satellites*, 2005.
- ¹¹ Tachikawa, S. et al. “Development of a Variable Emittance Radiator Based on a Perovskite Manganese Oxide”, *Journal of Thermophysics and Heat Transfer*, Vol. 17. No. 2, 2003, pp. 264 - 268.
- ¹² Kats, M. A. et al. “Vanadium dioxide as a natural disordered metamaterial: Perfect thermal emission and large broadband negative differential thermal emittance”, *Physical Review X*, Vol. 3, No. 041004, 2014.
- ¹³ Athanasopoulos, N., and Siakavellas, J. N., “Smart Patterned Surfaces with Programmable Thermal Emissivity and Their Design through Combinatorial Strategies”, *Scientific Reports*, Vol. 7, No. 12908, 2017.
- ¹⁴ Athanasopoulos, N., and Siakavellas, J. N., “Programmable thermal emissivity structures based on bioinspired self-shape materials”. *Scientific Reports*, Vol. 5, No. 17682, 2015.
- ¹⁵ Athanasopoulos, N., and Siakavellas, J. N., “Self-shape structures with programmable thermal radiative properties”, *Conference: Multifunctional Materials & Structures / Gordon Research*, Poster No. 3, 2016.
- ¹⁶ Momeni, F., M. Mehdi Hassani, N. S., Liu, X., and Ni, J., “A review of 4D printing”, *Materials and Design*, Vol. 122, 2017, pp. 42–79.
- ¹⁷ Erb, R. M., Sander, J. S., Grisch, R. and Studart, A. R., “Self-shaping composites with programmable bioinspired microstructures”, *Nature Communications*, Vol. 4, No. 1712, 2013.
- ¹⁸ Audoly, B., and Pomeau, Y., *Elasticity and Geometry*, Oxford university press, 2010.
- ¹⁹ Czernik, S., “Design of the Thermal Control System for Compass-1 Design of the Thermal Control System for Compass-1”, 2004.
- ²⁰ Scholz, A., König, F., Fröhlich, S., and Piepenbrock, J., “Flight Results of the COMPASS-1 Mission”, *Acta Astronautica*, Vol. 67, 2010, pp. 1289-1298.